

Robust measurement of wave function topology on NISQ quantum computers

Xiao Xiao,^{1,*} J. K. Freericks,^{2,†} and A. F. Kemper^{1,‡}

¹Department of Physics, North Carolina State University, Raleigh, North Carolina 27695, USA

²Department of Physics, Georgetown University, 37th and O Sts. NW, Washington, DC 20057 USA

(Dated: February 1, 2022)

Topological quantum phases of quantum materials are defined through their topological invariants. These topological invariants are quantities that characterize the global geometrical properties of the quantum wave functions and thus are immune to local noise. Here, we present a general strategy to measure topological invariants on NISQ quantum computers and demonstrate our proposal by applying it to a topological superconducting model. Remarkably, we find that the Chern numbers of the model can be measured exactly; that is, it is immune to the noise of NISQ machines. We also evaluate the Zak phase and ensemble geometric phase, which are not as robust as the Chern number, but still can be used to qualitatively distinguish different topological phases. Our study demonstrates that the robust nature of wave function topology allows noisy NISQ machines to determine topological invariants accurately.

Introduction — Topological phases are characterized by nonlocal topological invariants, which are by nature robust against local perturbations [1–21]. This unique property makes topological phases an ideal application of quantum computing, in particular in the NISQ era where the noise levels are high. A significant amount of work has been performed on realizing topological phases and identifying different topological phases *qualitatively* on quantum hardware [22–27]. However, although the strategies for calculating topological invariants are well-established in the condensed matter community, there have only been a few studies employing real quantum circuits to determine them [28–31].

The difficulty in using NISQ hardware to measure topological invariants stems from the inherent errors due to the non-fault-tolerant quantum hardware; the issues of noise are omnipresent within NISQ hardware calculations [32], and advanced error mitigation strategies often have to be deployed before *semiquantitative* results are obtained [33, 34]. These strategies may not suffice; the quantitative results may be significantly off from the exact results, regardless of the error mitigation. Even to obtain qualitatively correct results, a limitation to few qubits and low-depth circuits [35–37] is necessary to reduce the influence of the operation errors in NISQ quantum computers.

Here we develop quantum circuits—based on holonomy—that can measure topological invariants of models, and do so in a noise-resistant (or even noise-free) manner. Our strategy is to construct a general quantum circuit to measure the parallel transport of the wavefunction in the base space. These determine the connection of the wavefunction bundle, which permits the calculation of topological invariants in a gauge-invariant fashion. We demonstrate this idea by showing how to measure the

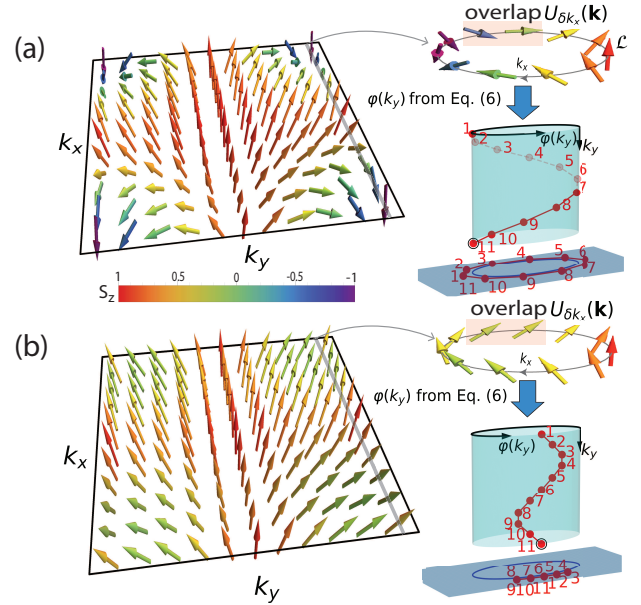


FIG. 1: Illustration of different topology of wave functions: the pseudo-spin representation of the wave function of a chiral p -wave superconductor in (a) the case of a topological phase and (b) the case of a trivial phase. The pseudo-spin vector field for a particular k_y (along the gray lines) determines the Zak phase $\phi(k_y)$, which has non-trivial (trivial) winding for the topological (trivial) phase. The central quantity here is the overlap of the wave function after a small transport in \mathbf{k} -space denoted by $U_{\delta \mathbf{k}}(\mathbf{k})$.

Chern number, the winding of the Zak phase, and the ensemble geometric phase (a density matrix generalization of the Zak phase) for a model of chiral p -wave superconductors. Strikingly, the Chern number can be measured *exactly* on NISQ hardware without any error, even when the system is tuned close to a topological phase transition. We are not aware of any other error-free measurements obtained from NISQ hardware. The winding of the Zak phase and ensemble geometric phase are less robust, but can still qualitatively determine different topological

*Electronic address: phxxiao@gmail.com

†Electronic address: james.freericks@georgetown.edu

‡Electronic address: akemper@ncsu.edu

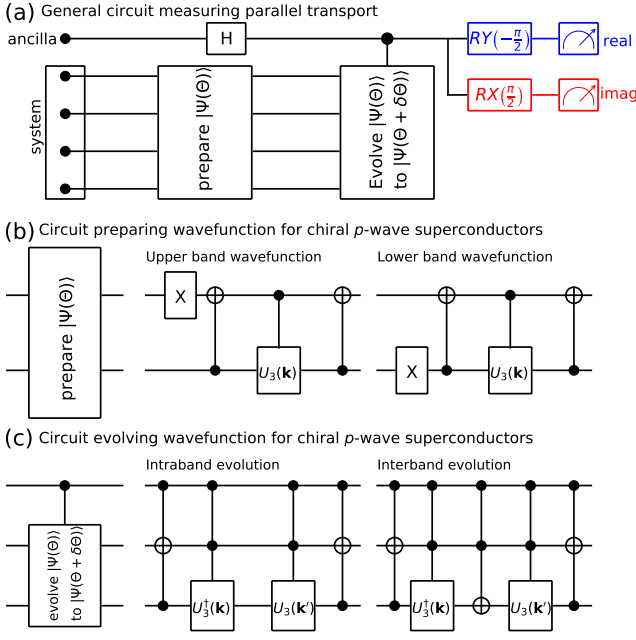


FIG. 2: Quantum circuit for measuring parallel transport of the wavefunction: (a) Schematic quantum circuit structure (independent of the details of the microscopic model); (b) Detailed circuit for wave-function preparation of the chiral p -wave superconductor [40]; and (c) Detailed circuit for wave-function evolution of the chiral p -wave superconductor [40]. In the panels, $U_3(\mathbf{k})$ (and $U_3^\dagger(\mathbf{k})$) denotes the general single-qubit operator specified by three angles determined at the momentum point \mathbf{k} , ‘X’ denotes a Pauli-X gate, ‘H’ is a Hadamard gate, ‘•’ denotes a controlled gate, and \oplus denotes a NOT gate.

phases.

General scheme and quantum circuits — To measure the topology of the wavefunction in some parameter space, the central quantity we use is the holonomy in the wavefunction bundle, which can be obtained by the parallel transportation of the wavefunction along a closed loop in parameter space. Topological states have non-trivial holonomy, while trivial states have trivial holonomy (see Fig. 1 for examples). Along a closed path, each parallel transport operation defines a local connection, which is determined from the overlap of the wavefunctions $\langle \Psi_\Theta | \Psi_{\Theta+\delta\Theta} \rangle$ at two neighboring points Θ and $\Theta+\delta\Theta$ in the parameter space. Therefore, the key step to measure the holonomy with quantum circuits is to characterize the local wavefunction overlap, which requires the evolution of the wavefunction from $|\Psi_\Theta\rangle$ to $|\Psi_{\Theta+\delta\Theta}\rangle$. Once this is known, the overlap $\langle \Psi_\Theta | \Psi_{\Theta+\delta\Theta} \rangle$ can be evaluated by a Hadamard test algorithm (see Fig. 2 (a)).

So far our procedure stated in the above is general and largely independent of model details. To demonstrate an explicit realization, we use the two-dimensional chiral p -wave superconductor model [38, 39], which can be tuned through several trivial and topological phases. Our aim is to identify phases by the topology of their wave

functions. This model can be described by the following Hamiltonian density:

$$\mathcal{H}(\mathbf{k}) = \Delta(\sin k_y \sigma_x + \sin k_x \sigma_y) - [t(\cos k_x + \cos k_y) + \mu] \sigma_z, \quad (1)$$

where Δ is the superconducting gap, t is the nearest neighbor hopping amplitude, and $\mu + 2t$ is the chemical potential in the normal state. We set $t = \Delta = 1$ so that the different phases are tuned by the parameter μ only. The topological quantum critical points occur when the energy levels of the two bands touch at some point in \mathbf{k} -space. As shown in Fig. 3, this model exhibits 4 different phases separated by 3 topological quantum critical points at $\mu = \{-2, 0, 2\}$. The trivial phases with $\mathcal{C} = 0$ occur for $|\mu| > 2$; when $|\mu| < 2$, $\mathcal{C} = \text{sign}(\mu)$.

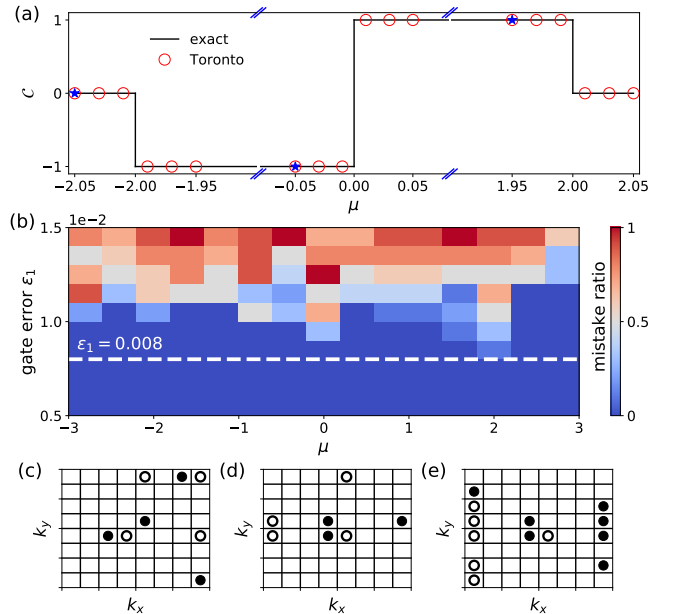


FIG. 3: Robustness of the Chern number on NISQ hardware: (a) Topological phase diagram for the chiral p -wave superconductor. The Chern number, measured on IBMQ-Toronto, is shown with open symbols falling accurately on the exact results. (b) Mistake ratio of Chern number measurements from noisy simulations (we assume that the two-qubit gate error ε_2 is 10 times the one-qubit gate error ε_1). (c)-(e) Integer gauge field $n(\mathbf{k})$ extracted from the data points denoted by blue stars in (a) (• denotes $n = 1$, ○ denotes $n = -1$ and the empty box is for $n = 0$). The overlap $U_{\delta\mathbf{k}}(\mathbf{k})$ measured by both IBMQ-Toronto and noisy simulations was obtained with $N = 5120$ shots.

The Chern number — The Chern number for a particular μ can be obtained by discretizing the Brillouin zone (BZ) and measuring the normalized overlap $U_{\delta\mathbf{k}}(\mathbf{k}) \equiv \langle \Psi(\mathbf{k}) | \Psi(\mathbf{k} + \delta\mathbf{k}) \rangle / |\langle \Psi(\mathbf{k}) | \Psi(\mathbf{k} + \delta\mathbf{k}) \rangle|$ between neighboring mesh points following the general strategy described in the last section. Explicitly, the Chern number can be expressed by the measured overlap in a gauge-invariant

way [41]:

$$\mathcal{C} = \frac{1}{2\pi i} \sum_{\mathbf{k}} \mathcal{F}(\mathbf{k}), \quad (2)$$

where:

$$\begin{aligned} \mathcal{F}(\mathbf{k}) = & \ln [U_{\delta k_x}(\mathbf{k}) U_{\delta k_y}(\mathbf{k} + \delta k_x \hat{x}) \\ & \times U_{\delta k_x}^{-1}(\mathbf{k} + \delta k_y \hat{y}) U_{\delta k_y}^{-1}(\mathbf{k})], \end{aligned} \quad (3)$$

where \hat{x}, \hat{y} are unit vectors in the x and y directions in the BZ. From this definition, we have $-\pi < \mathcal{F}(\mathbf{k})/i \leq \pi$. The success of the calculations largely relies on the admissibility condition $|\mathcal{F}(\mathbf{k})| \leq \pi$ [41]. The quantity $\mathcal{F}(\mathbf{k})$ approaches the continuum value of field strength $F(\mathbf{k})\delta k_x \delta k_y = \nabla \times \mathbf{A}(\mathbf{k}) \cdot \hat{z} \delta k_x \delta k_y$, where $\mathbf{A}(\mathbf{k})$ is the Berry curvature, when $\delta \mathbf{k} \rightarrow 0$. As long as there is a finite gap between the two bands, $\mathcal{F}(\mathbf{k})$ should be small for a sufficiently dense mesh so that the Chern number calculated from the lattice is identical to the continuum value. A finite critical mesh density, above which the Chern number calculated from lattice is identical to the continuum value, can be determined by a breaking of the admissibility condition [41]. Typically for Chern number $\mathcal{C} \sim \mathcal{O}(1)$, the critical mesh number is not very large. In our simulations, we will demonstrate our proposal by using a uniform discretization of the BZ into 8×8 mesh points.

We first demonstrate the measurement of the Chern number on the IBMQ-Toronto machine [42], focusing on the regions near the topological critical points, which are typically most sensitive to noise. Fig. 3(a) shows the exact results for the Chern number \mathcal{C} as the chemical potential is varied. The plot shows only the regions near the phase transitions, where we have performed calculations on the quantum computer. Remarkably, we observe that the Chern number is *error-free*. This vividly demonstrates the power of global properties of the wavefunction, which are by definition independent of any local deformation.

To investigate the robustness of the Chern number measurement, we performed a noise analysis by varying the gate errors. For typical noise in the IBMQ machines, the two-qubit gate error ε_2 is about one order of magnitude larger than that of the one-qubit gate error ε_1 . In our simulation, we simply set $\varepsilon_2 = 10\varepsilon_1$ and vary only the one-qubit gate error ε_1 . The one-qubit gate error ε_1 is successively tuned from $\varepsilon_1 = 0.005$ to $\varepsilon_1 = 0.015$ with step size 0.001, and for each gate error 10 trials were performed. The mistake ratio of the measurement is thus defined as the percentage of mistakes in these 10 trials. The results of the noisy simulations are shown in Fig. 3(b). As expected, larger gate error leads to a larger mistake ratio. The measured Chern number is error-free when $\varepsilon_1 \leq 0.008$, and this noise level can be achieved in NISQ machines. We have to note that our measurement scheme plays an important role in leading to the error-free result. In our measurement scheme,

$U_{\delta \mathbf{k}}(\mathbf{k})$ at each discretized momentum point is measured by the quantum circuit of the same structure, so the error at each momentum point is contributed by two parts: one from parameter-relevant operations, and the other from parameter-independent operations. By performing phase measurements, the parameter-independent part is gauged out, so our measurement scheme improves the error tolerance.

A different perspective on the results may be obtained by rewriting Eq. (3) as:

$$\begin{aligned} \mathcal{F}(\mathbf{k}) = & [\ln U_{\delta k_x}(\mathbf{k}) - \ln U_{\delta k_x}(\mathbf{k} + \delta k_y \hat{y})] \\ & + [\ln U_{\delta k_y}(\mathbf{k} + \delta k_x \hat{x}) - \ln U_{\delta k_y}(\mathbf{k})] + 2\pi i n(\mathbf{k}). \end{aligned} \quad (4)$$

Here, $|n(\mathbf{k})| \leq 2$ is an integer-valued field that acquires a non-zero value whenever $\mathcal{F}(\mathbf{k})$ moves out of the principal branch of the logarithm. Precisely where and how often this occurs depends sensitively on the measurement and its associated noise. Inserting Eq.(4) into the expression of the Chern number (Eq.(2)), one finds:

$$\mathcal{C} = \sum_{\mathbf{k}} n(\mathbf{k}). \quad (5)$$

From the measured overlaps $U_{\delta \mathbf{k}}(\mathbf{k})$, we can extract the distribution of $n(\mathbf{k})$ for three typical μ values (denoted by the blue stars in Fig. 3(b)-(d)), and we show them in Fig. 3(e)-(g). The sum of the integer-valued field yields results which are consistent with Eq.(5). Note that each calculation will yield different integer fields, but these always conspire to achieve the correct net value when summed [41].

Winding of the Zak phase — Another way to determine the topology of the wavefunction is to measure the winding of the Zak phase, which is defined by parallel transport of the wavefunction in only one direction of the Brillouin zone (as opposed to measuring the transport summed over the entire Brillouin zone for the Chern number). The Zak phase measures the holonomy of the wavefunction in one direction and can be written in terms of normalized overlap $U_{\delta k_x}(\mathbf{k})$ as:

$$\varphi(k_y) = \ln \prod_{\mathbf{k} \in \mathcal{L}(k_y)} U_{\delta k_x}(\mathbf{k}), \quad (6)$$

where $\mathcal{L}(k_y)$ is the loop for a fixed k_y along the k_x -direction. Then, as illustrated in Fig. 1, the winding of the Zak phase along the k_y -direction relates to the Chern number as follows:

$$\mathcal{C} = \frac{1}{2\pi} \oint dk_y \frac{d\varphi(k_y)}{dk_y}. \quad (7)$$

To obtain this from the quantum computer, we measure the normalized overlap $U_{\delta k_x}(\mathbf{k})$ by using the quantum circuits shown in Fig. 1, from which we can obtain the Zak phase for a particular k_y . In Fig. 4(a) and (b), the Zak phases $\varphi(k_y)$ obtained from 5 independent simulations on IBMQ-Toronto are shown as functions of k_y for

a typical topological state (panel (a) with $\mu = 1.9$) and a typical trivial state (panel (b) $\mu = 2.1$) respectively. Here, the results from the NISQ machines do not fall exactly on the exact results (the blue curves), but the results from quantum computers do capture the main features of the two topologically distinct phases. That is, for the topological state, a sharp change at the high-symmetry point $k_y = \pi$ (see Fig. 4(a)) can be identified and signifies the non-trivial winding of the Zak phase along k_y , while this sharp change is absent for the trivial phase as illustrated in Fig. 4(b). For comparison, we also performed noisy simulations with $\epsilon_1 = 0.008$ and $\epsilon_2 = 10\epsilon_1$ for the same parameters. The results of 5 independent trials for the topological state with $\mu = 1.9$ (non-trivial) and $\mu = 2.1$ (trivial) are shown in Fig. 4(c) and the (d), respectively. It can be clearly observed that the noisy simulation results are quite similar to those from the IBMQ-Toronto quantum computer. These results from the quantum computer and the noisy simulations suggest that the topology of wavefunctions can also be successfully identified by measuring the winding of the Zak phase.

Ensemble geometric phase — Thus far we have demonstrated that the topology of the lowest lying energy band can be measured on NISQ machines. Here we further demonstrate that the quantum circuits proposed in Fig. 2 can be used to measure the topology of mixed states; these may arise from a finite temperature or by being driven out of equilibrium. The many-body generalization of the Zak phase in this case is the *ensemble geometric phase* φ_E introduced by Bardyn *et al.*[43] Unlike

other proposals such as the Uhlmann phase[44–46], the ensemble geometric phase reduces to the Zak phase in the thermodynamic limit. The ensemble geometric phase is obtained from a “fictitious Hamiltonian G ,” which for Bloch states coincides with the real Hamiltonian scaled by $\beta = 1/T$:

$$G = \sum_{\mathbf{k}} G_{\mathbf{k}} c_{\mathbf{k}}^\dagger c_{\mathbf{k}} = \sum_{\mathbf{k}} \beta H_{\mathbf{k}} c_{\mathbf{k}}^\dagger c_{\mathbf{k}}. \quad (8)$$

The ensemble geometric phase is obtained from the rotation matrices $\mathcal{U}_{\mathbf{k}}$ that diagonalize $G_{\mathbf{k}}$ [43]:

$$\varphi_E(k_y) = \Im m [\ln \det (1 + M_T)], \quad (9)$$

where the matrix M_T is constructed as follows: first create

$$B_{\mathbf{k}} = \text{diag}_s(\lambda_{\mathbf{k},s}) := \mathcal{U}_{\mathbf{k}}^\dagger G_{\mathbf{k}} \mathcal{U}_{\mathbf{k}}, \quad (10)$$

which is the diagonal matrix of eigenvalues $\lambda_{\mathbf{k},s}$ of $G_{\mathbf{k}}$, and then form

$$M_T = (-1)^{N_L+1} \prod_{\mathbf{k} \in \mathcal{L}(k_y)} e^{-B_{\mathbf{k}}} \mathcal{U}_{\mathbf{k}+\delta\mathbf{k}_x\hat{x}}^\dagger \mathcal{U}_{\mathbf{k}}. \quad (11)$$

Here N_L is the number of grid points along the loop $\mathcal{L}(k_y)$. In the evaluation of M_T , the important component is the product $\mathcal{U}_{\mathbf{k}+\delta\mathbf{k}_x\hat{x}}^\dagger \mathcal{U}_{\mathbf{k}}$, which includes the parallel transport of both intraband and interband wavefunctions. For the model of a chiral p -wave superconductor, these parallel transports can be measured by the quantum circuits shown in Fig. 2(b) and (c).

The factor $e^{-B_{\mathbf{k}}} = \text{diag}_s(e^{-\lambda_{\mathbf{k},s}})$ along the loop $\mathcal{L}(k_y)$ has crucial effects on mixed states. The lowest purity band (separated from others by a purity gap) has the highest weight according to the factor $e^{-B_{\mathbf{k}}}$. Therefore, if the number of grid points is large enough, the ensemble geometric phase approaches the Zak phase. The deviation of the ensemble geometric phase φ_E from the Zak phase φ is proportional to $(T/N_L)^2$ [43]. Therefore, for small N_L the topology of the density matrix is correctly measured as long as T is small compared to the energy gap.

We demonstrate the measurement of the ensemble geometric phase by noisy simulations, which (as was shown in Figs. 3 and 4) have results compatible with those from real quantum hardware. The winding of the ensemble geometric phase for the topological phase with $\mu = 1.9$ and for the trivial phase with $\mu = 2.1$ is shown in Fig. 5(a) and (b), respectively. Indeed, the results are similar to that of the Zak phase as expected, and likewise the two phases with different topology can be qualitatively distinguished. Note that the challenge with performing this calculation on a NISQ machine is actually the initial thermal state preparation at low temperature.

Discussion and conclusion — Although we illustrate the application of our method to a non-interacting model, whose wavefunction can be easily prepared, the principles

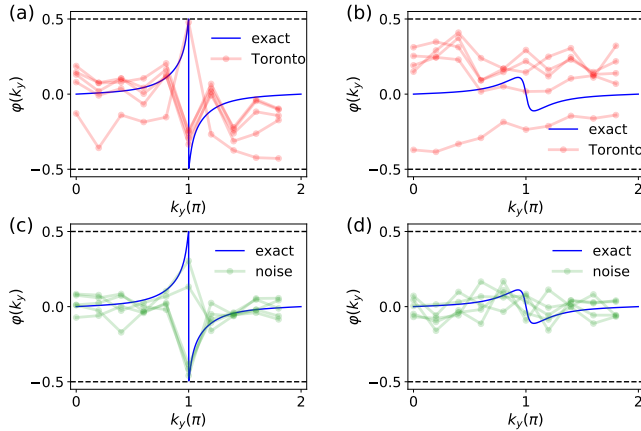


FIG. 4: Qualitative robustness of Zak phase on NISQ machines: the winding of Zak phase $\varphi(k_y)$ along k_y measured by IBMQ-Toronto: (a) topological phase with $\mu = 1.9$; (b) trivial phase with $\mu = 2.1$. For the comparison, the winding of Zak phase was measured by noisy simulations and shown in (c) for $\mu = 1.9$ and (d) for $\mu = 2.1$. In the noisy simulations, the gate noises were chosen to be $\epsilon_1 = 0.008$ and $\epsilon_2 = 0.08$. Each overlap $U_{\delta\mathbf{k}}(\mathbf{k})$ measured by IBMQ-Toronto and noisy simulations were obtained with $N = 5120$ shots, and $N_L = 8$ grids point were used for each loop $\mathcal{L}(k_y)$ to obtain the Zak phase.

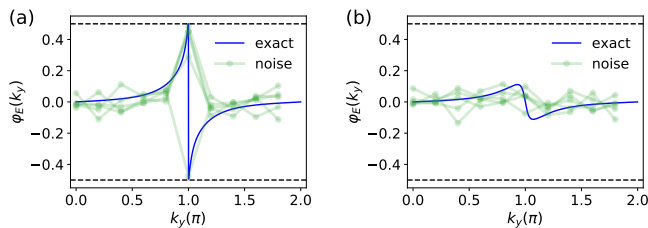


FIG. 5: Qualitative robustness of the ensemble geometric phase illustrated by noise simulations: (a) the winding of ensemble geometric phase $\varphi_E(k_y)$ along k_y for (a) topological phase with $\mu = 1.9$ and (b) trivial phase with $\mu = 2.1$. The number of grid for the loop $\mathcal{L}(k_y)$ is $N_L = 8$ and the inverse temperature $\beta = 2.1$. In this simulation, the gate noises were chosen to be $\epsilon_1 = 0.008$ and $\epsilon_2 = 0.08$, and $N = 5120$ shots were used to obtain each element of $\mathcal{U}_{\mathbf{k}+\delta\mathbf{k}_x\hat{x}}^\dagger \mathcal{U}_{\mathbf{k}}$ in Eq.(11).

stated here can be generally applied to interacting topological models. Following the discussion in Ref. [2], the topology of a wave function can be measured in a real-space calculation by examining the evolution of the wave function under the variation of a twisted boundary condition angle, even when the system is interacting. Taking $2D$ systems as an example, as we considered in this work, the two twist angles at the boundaries along the x and y directions (θ_x, θ_y) form a 2-torus exactly like the 2-torus formed by (k_x, k_y) of the chiral p -wave superconductor. As such, the parallel transport for the more complex models is simple to achieve, and all the machinery developed in this work can be applied straightforwardly to measure the wavefunction topology on quantum hardware.

A comparison between our method with the recently proposed scheme [47] to measure the many-body Chern number by randomized measurements is in order. First, the randomized measurement scheme is based on decomposing the wavefunction manifold and requires the prepa-

ration of two copies of the wavefunction for a given set of parameters in the base space. In contrast, in our algorithm, we only use one copy. Second, the many-body Chern number in Ref. [47] is inferred from the winding of the measured expectation of the SWAP applied to the two copies of the wavefunction after ‘surgery’, while our method can either measure the Chern number directly or infer it from the winding of the Zak phase. More importantly, as we have shown here, although it is not difficult to qualitatively identify different winding properties on NISQ hardware, it is generally difficult to do so quantitatively. The randomized measurement scheme has yet to be carried out on NISQ machines.

In conclusion, by measuring the Chern number, the winding of the Zak phase and the winding of the ensemble geometric phase for chiral p -wave superconductors, we demonstrated how the topology of a wavefunction can be measured, and that it is robust against operation errors of quantum computers in this NISQ era. Our work provides a general scheme to investigate various topologically ordered systems on current quantum hardware.

Acknowledgments

We acknowledge helpful discussions with Michael Geller. This work was supported by the Department of Energy, Office of Basic Energy Sciences, Division of Materials Sciences and Engineering under Grant No. DE-SC0019469. J.K.F. was also supported by the McDevitt bequest at Georgetown. We acknowledge use of the IBM Q for this work. The views expressed are those of the authors and do not reflect the official policy or position of IBM or the IBM Q team. Access to the IBM Q Network was obtained through the IBM Q Hub at NC State. We acknowledge the use of the QISKIT software package [48] for performing the quantum simulations.

-
- [1] D. J. Thouless, M. Kohmoto, M. P. Nightingale, and M. den Nijs, *Phys. Rev. Lett.* **49**, 105 (1982).
 - [2] Q. Niu, D. J. Thouless, and Y.-S. Wu, *Phys. Rev. B* **31**, 3372 (1985).
 - [3] D. N. Sheng, L. Sheng, and Z. Y. Weng, *Phys. Rev. B* **73**, 233406 (2006).
 - [4] H. Obuse, A. Furusaki, S. Ryu, and C. Mudry, *Phys. Rev. B* **76**, 075301 (2007).
 - [5] J. Li, R.-L. Chu, J. K. Jain, and S.-Q. Shen, *Phys. Rev. Lett.* **102**, 136806 (2009).
 - [6] E. Prodan, *J. Phys. A: Math. Theor.* **44**, 113001 (2011).
 - [7] J. T. Chalker, M. Ortuno, and A. M. Somoza, *Phys. Rev. B* **83**, 115317 (2011).
 - [8] J. Liu, A. C. Potter, K. T. Law, and P. A. Lee, *Phys. Rev. Lett.* **109**, 267002 (2012).
 - [9] A. M. Lobos, R. M. Lutchyn, and S. Das Sarma, *Phys. Rev. Lett.* **109**, 146403 (2012).
 - [10] E. J. König, P. M. Ostrovsky, I. V. Protopopov, I. V. Gornyi, I. S. Burmistrov, and A. D. Mirlin *Phys. Rev. B* **88**, 035106 (2013).
 - [11] A. Altland, D. Bagrets, L. Fritz, A. Kamenev, and H. Schmiedt, *Phys. Rev. Lett.* **112**, 206602 (2014).
 - [12] I. M. Shem, T. L. Hughes, J. Song, and E. Prodan, *Phys. Rev. Lett.* **113**, 046802 (2014).
 - [13] J. Song, and E. Prodan, *Phys. Rev. B* **89**, 224203 (2014).
 - [14] M. Foster, H.-Y. Xie, and Y.-Z. Chou, *Phys. Rev. B* **89**, 155140 (2014).
 - [15] J. Wang, B. Liao, and S.-C. Zhang, *Phys. Rev. B* **89**, 085106 (2014).
 - [16] C. Liu, W. Gao, B. Yang, and S. Zhang, *Phys. Rev. Lett.* **119**, 183901 (2017).
 - [17] E. J. Meier, F. A. An, A. Dauphin, M. Maffei, P. Massignan, T. L. Hughes, B. Gadway, *Science* **362**, 929 (2018).
 - [18] S. Stutz, Y. Plotnik, Y. Lumer, P. Titum, N. Linder, M. Segev, M. C. Rechtsman, and A. Szameit, *Nature* **560**, 461 (2018).

- [19] X. Xiao, [arXiv:1802.02687 \(2018\)](#).
- [20] O. Shtanko, and R. Movassagh, *Phys. Rev. Lett.* **121**, 126803 (2018).
- [21] T. Okugawa, P. Tang, A. Rubio, and D. Kennes, *Phys. Rev. B* **102**, 201405(R) (2020).
- [22] P. Roushan, C. Neill, Yu Chen, M. Kolodrubetz, C. Quintana, N. Leung, M. Fang, R. Barends, B. Campbell, Z. Chen, B. Chiaro, A. Dunsworth, E. Jeffrey, J. Kelly, A. Megrant, J. Mutus, P. J. J. O'Malley, D. Sank, A. Vainsencher, J. Wenner, T. White, A. Polkovnikov, A. N. Cleland and J. M. Martinis *Nature* **515**, 241 (2014).
- [23] K. Choo, C. W. von Keyserlingk, N. Regnault, and T. Neupert, *Phys. Rev. Lett.* **121**, 086808 (2018).
- [24] A. Smith, B. Jobst, A. G. Green, and F. Pollmann, [arXiv:1910.05351 \(2019\)](#).
- [25] D. Azses, R. Haenel, Y. Naveh, R. Raussendorf, E. Sela, and E. G. D. Torre, *Phys. Rev. Lett.* **125**, 120502 (2020).
- [26] F. Mei, Q. Guo, Y.-F. Yu, L. Xiao, S.-L. Zhu, and S. Jia, *Phys. Rev. Lett.* **125**, 160503 (2020).
- [27] X. Xiao, J. K. Freericks, and A. F. Kemper, [arXiv:2006.05524 \(2020\)](#).
- [28] E. Flurin, V. V. Ramasesh, S. Hacohe-Gourgy, L. S. Martin, N. Y. Yao, and I. Siddiqi, *Phys. Rev. X* **7**, 031023 (2017).
- [29] X. Zhan, L. Xiao, Z. Bian, K. Wang, X. Qiu, B. Sanders, W. Yi, and P. Xue, *Phys. Rev. Lett.* **119**, 130501 (2017).
- [30] X.-Y. Xu, Q.-Q. Wang, W.-W. Pan, K. Sun, J.-S. Xu, G. Chen, J.-S. Tang, M. Gong, Y.-J. Han, C.-F. Li, and G.-C. Guo, *Phys. Rev. Lett.* **120**, 260501 (2018).
- [31] A. Elben, J. Yu, G. Zhu, M. Hafezi, F. Pollmann, P. Zoller, and B. Vermersch, *Sci. Adv.* **6**, eaaz3666 (2020).
- [32] J. Preskill, *Quantum* **2**, 79 (2018).
- [33] A. Kandala, K. Temme, A. D. Corcoles, A. Mezzacapo, J. M. Chow, and J. M. Gambetta, *Nature* **567**, 491 (2019).
- [34] K. E. Hamilton, and R. C. Pooser, *Quantum Machine Intelligence* **2**, 10 (2020).
- [35] A. Cervera-Lierta, *Quantum* **2**, 114 (2018).
- [36] K. Yeter-Aydeniz, R. C. Pooser, and G. Siopsis, *npj Quantum Inf.* **6**, 63 (2020).
- [37] H. R. Grimsley, S. E. Economou, E. Barnes, and N. J. Mayhall, *Nat. Commun.* **10**, 3007 (2019).
- [38] G. E. Volovik, *JETP Lett.* **70**, 609 (1999).
- [39] N. Read, and D. Green, *Phys. Rev. B* **61**, 10267 (2000).
- [40] See the appendix for the details of quantum circuit constructions for the chiral p -wave superconducting model.
- [41] T. Fukui, Y. Hutsugai, and H. Suzuki, *J. Phys. Soc. Jpn.* **74**, 1674 (2005).
- [42] IBM Q team, “IBM Q Toronto backend specification v1.0.7,” retrieved from <https://quantum-computing.ibm.com> (2020).
- [43] C.-E. Bardyn, L. Wawer, A. Altland, M. Fleischhauer, and S. Diehl, *Phys. Rev. X* **8**, 011035 (2018).
- [44] Z. Huang, and D. P. Arovas, *Phys. Rev. Lett.* **113**, 076407 (2014).
- [45] O. Viyuela, A. Rivasand, and M. A. Martin-Delgado, *Phys. Rev. Lett.* **112**, 130401 (2014).
- [46] O. Viyuela, A. Rivasand, and M. A. Martin-Delgado, *Phys. Rev. Lett.* **113**, 076408 (2014).
- [47] Z.-P. Cian, H. Dehghani, A. Elben, B. Vermersch, G. Zhu, M. Barkeshli, P. Zoller, and M. Hafezi, [arXiv:2005.13543 \(2020\)](#).
- [48] G. Aleksandrowicz, *et al.* Qiskit: An open-source framework for quantum computing. <https://doi.org/10.5281/ZENODO.2562111> (2019).

Appendix A: Details of quantum circuits construction for chiral p -wave superconductors

We consider how to measure the overlap of the wavefunctions at neighbored mesh points by the standard Hadamard test. To do so we denote the prepared state as $|\Psi\rangle = |0\rangle \otimes |\psi\rangle$, where $|0\rangle$ is the initial state of the ancilla and $|\psi\rangle$ is the wavefunction at one of the mesh points in the BZ. Then we first apply the Hadamard gate to the ancilla and resulting in the following product state:

$$|\Psi\rangle = \frac{1}{\sqrt{2}}|0\rangle \otimes |\psi\rangle + \frac{1}{\sqrt{2}}|1\rangle \otimes |\psi\rangle. \quad (\text{A1})$$

Then, we impose the controlled \mathcal{U} operation, where \mathcal{U} relates the wavefunctions at the neighboring mesh points. After applying the operation, the state is in an entangled superposition given by

$$|\Psi\rangle = \frac{1}{\sqrt{2}}|0\rangle \otimes |\psi\rangle + \frac{1}{\sqrt{2}}|1\rangle \otimes \mathcal{U}|\psi\rangle. \quad (\text{A2})$$

Then we projectively measure the expectations of $\sigma_x \otimes I$ and $\sigma_y \otimes I$, which will give the real part and imaginary parts of the overlap:

$$\langle \sigma_x \otimes I \rangle = \frac{1}{2} [\langle 0| \otimes \langle \psi| + \langle 1| \otimes \langle \psi| \mathcal{U}^\dagger] \sigma_x \otimes I [|0\rangle \otimes |\psi\rangle + |1\rangle \otimes \mathcal{U}|\psi\rangle] = \frac{1}{2} [\langle \psi| \mathcal{U}|\psi\rangle + \langle \psi| \mathcal{U}^\dagger|\psi\rangle] = \Re \langle \psi| \mathcal{U}|\psi\rangle, \quad (\text{A3})$$

and

$$\langle \sigma_y \otimes I \rangle = \frac{1}{2} [\langle 0| \otimes \langle \psi| + \langle 1| \otimes \langle \psi| \mathcal{U}^\dagger] \sigma_y \otimes I [|0\rangle \otimes |\psi\rangle + |1\rangle \otimes \mathcal{U}|\psi\rangle] = -\frac{i}{2} [\langle \psi| \mathcal{U}|\psi\rangle - \langle \psi| \mathcal{U}^\dagger|\psi\rangle] = \Im m \langle \psi| \mathcal{U}|\psi\rangle. \quad (\text{A4})$$

To complete the algorithm, we have two more steps: first, we need to determine what the initial state $|\psi\rangle$ is that we will use and how we prepare it by a quantum circuit and second, we need to determine the unitary operator \mathcal{U} that evolves the wavefunction between neighboring mesh points and how we can realize it by quantum circuits. We next answer these two questions in turn.

1. Preparation of wave function

We begin from the Hamiltonian density given by Eq. (1) of the main text. The full Hamiltonian can be written as:

$$H = \sum_{\mathbf{k}} \begin{pmatrix} c_{\mathbf{k}}^\dagger & d_{\mathbf{k}}^\dagger \end{pmatrix} \mathcal{H}(\mathbf{k}) \begin{pmatrix} c_{\mathbf{k}} \\ d_{\mathbf{k}} \end{pmatrix}, \quad (\text{A5})$$

where $\mathcal{H}(\mathbf{k})$ is given by Eq. (1). $\mathcal{H}(\mathbf{k})$ has the eigenvalues:

$$E_{\pm} = \pm \sqrt{\Delta^2 (\sin^2 k_y + \sin^2 k_x) + [t(\cos k_x + \cos k_y) + \mu]^2}. \quad (\text{A6})$$

By setting $\Delta = t = 1$ as it is assumed in the main text, we find that the gap between the two energy bands would be close at $(k_x = 0, k_y = 0)$ for $\mu = -2$, at $(k_x = \pm\pi, k_y = \pm\pi)$ for $\mu = -2$, and at $(k_x = \pm\pi, k_y = \mp\pi)$ for $\mu = 0$. These gap closing points separate different topological phases.

We define angles $\theta(\mathbf{k})$ and $\varphi(\mathbf{k})$ determined at each momentum point:

$$\cos \theta = \frac{t(\cos k_x + \cos k_y) + \mu}{E_+}, \quad (\text{A7})$$

and

$$\cos \varphi = \frac{\Delta \sin k_y}{\sqrt{\Delta^2 (\sin^2 k_y + \sin^2 k_x)}}, \quad (\text{A8})$$

so that the corresponding eigenstates of E_{\pm} can be written as:

$$\Psi_+(\mathbf{k}) = \begin{pmatrix} \cos \theta/2 \\ \sin \theta/2 e^{-i\varphi} \end{pmatrix}, \quad \Psi_-(\mathbf{k}) = \begin{pmatrix} -\sin \theta/2 e^{i\varphi} \\ \cos \theta/2 \end{pmatrix}. \quad (\text{A9})$$

This eigensolution indicates that:

$$\text{diag}(E_+(\mathbf{k}), E_-(\mathbf{k})) = V^\dagger(\mathbf{k}) \mathcal{H}(\mathbf{k}) V(\mathbf{k}), \quad (\text{A10})$$

where $V = [\Psi_+, \Psi_-]$. We denote this diagonalized representation formed by the eigenstates of $\mathcal{H}(\mathbf{k})$ as the band representation, and the corresponding annihilation operators for the E_+ and E_- bands are $f_{\mathbf{k}}$ and $g_{\mathbf{k}}$. They relates to $c_{\mathbf{k}}$ and $d_{\mathbf{k}}$ as:

$$\begin{pmatrix} f_{\mathbf{k}} \\ g_{\mathbf{k}} \end{pmatrix} = V^\dagger \begin{pmatrix} c_{\mathbf{k}} \\ d_{\mathbf{k}} \end{pmatrix}. \quad (\text{A11})$$

The topological invariant is calculated from the wavefunction in the Brillouin zone. Therefore, we can begin from the diagonalized band representation. The initial states are either $|0_f 1_g\rangle$ for the valence band or $|1_f 0_g\rangle$ for the conducting band. The wavefunction in the Brillouin zone can be constructed by the creation operators $c_{\mathbf{k}}^\dagger$ and $d_{\mathbf{k}}^\dagger$ from vacuum. The relation between $(f_{\mathbf{k}}, g_{\mathbf{k}})$ and $(c_{\mathbf{k}}, d_{\mathbf{k}})$ is clear from Eq. (A11), or more explicitly

$$\begin{cases} c_{\mathbf{k}}^\dagger = \cos \frac{\theta}{2} f_{\mathbf{k}}^\dagger - \sin \frac{\theta}{2} e^{-i\varphi} g_{\mathbf{k}}^\dagger, \\ d_{\mathbf{k}}^\dagger = \sin \frac{\theta}{2} e^{i\varphi} f_{\mathbf{k}}^\dagger + \cos \frac{\theta}{2} g_{\mathbf{k}}^\dagger. \end{cases} \quad (\text{A12})$$

Therefore, the following relation can be found that relates the two representations by a unitary operator:

$$\begin{pmatrix} |0_c 0_d\rangle \\ |1_c 0_d\rangle \\ |0_c 1_d\rangle \\ |1_c 1_d\rangle \end{pmatrix} = \begin{pmatrix} 1 & 0 & 0 & 0 \\ 0 & \cos \frac{\theta}{2} & -\sin \frac{\theta}{2} e^{-i\varphi} & 0 \\ 0 & \sin \frac{\theta}{2} e^{i\varphi} & \cos \frac{\theta}{2} & 0 \\ 0 & 0 & 0 & 1 \end{pmatrix} \begin{pmatrix} |0_f 0_g\rangle \\ |1_f 0_g\rangle \\ |0_f 1_g\rangle \\ |1_f 1_g\rangle \end{pmatrix} = U(\theta, \varphi) \begin{pmatrix} |0_f 0_g\rangle \\ |1_f 0_g\rangle \\ |0_f 1_g\rangle \\ |1_f 1_g\rangle \end{pmatrix}. \quad (\text{A13})$$

From this relation, we know that the state $|\psi\rangle$ is obtained by applying U on either $|1_f 0_g\rangle$ for the conduction band or $|0_f 1_g\rangle$ for the valence band. This operation can be realized by two CNOT gates and a controlled- U_3 gate:

$$U(\theta, \varphi) = \text{CNOT}[q_1, q_0] \text{CU}_3[q_0, q_1](\vartheta = \theta, \lambda = -\varphi, \phi = \varphi) \text{CNOT}[q_1, q_0], \quad (\text{A14})$$

where the first qubit in the bracket is the control qubit and the second one is the target qubit. The matrix form of $\text{CU}_3[q_0, q_1](\vartheta, \lambda, \phi)$ is:

$$\text{CU}_3[q_0, q_1](\vartheta, \lambda, \phi) = \begin{pmatrix} 1 & 0 & 0 & 0 \\ 0 & \cos \frac{\vartheta}{2} & 0 & -\sin \frac{\vartheta}{2} e^{i\lambda} \\ 0 & 0 & 1 & 0 \\ 0 & e^{i\phi} \sin \frac{\vartheta}{2} & 0 & e^{i(\lambda+\phi)} \cos \frac{\vartheta}{2} \end{pmatrix}. \quad (\text{A15})$$

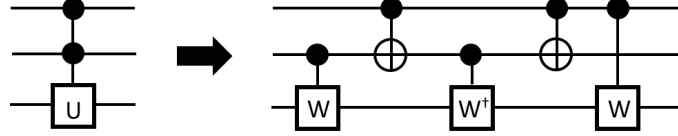


FIG. 6: The realization of the controlled-controlled-unitary gate by two-qubit gates, where W fulfills the condition: $W^2 = U$.

2. Relating wavefunctions at neighboring mesh points

From the discussion in the last subsection, we understand that the state at a particular point (k, t) in the Brillouin zone can be prepared by $U_b(\theta_{k,t}, \varphi_{k,t})$ for the valence ($b = v$) or conduction ($b = c$) band. Therefore, the operation transforming the wavefunction at (k, t) to that at (k', t') is

$$\mathcal{U}_{b,b'}(k', t'; k, t) = U_b(\theta_{k',t'}, \varphi_{k',t'}) U_{b'}^\dagger(\theta_{k,t}, \varphi_{k,t}). \quad (\text{A16})$$

To measure the overlap of the wavefunction, we use an ancilla qubit to control the application of $\mathcal{U}(k', t'; k, t)$ on the other two qubits. This means that the equation above is modified to

$$C\mathcal{U}(k', t'; k, t) = C\mathcal{U}(\theta_{k',t'}, \varphi_{k',t'}) C\mathcal{U}^\dagger(\theta_{k,t}, \varphi_{k,t}). \quad (\text{A17})$$

The extra letter C indicates that the two-qubit unitary operation is controlled by an ancilla qubit. For each CU operation, we can realize it by extending the two-qubit gate in Eq. (A7) as follows:

$$C\mathcal{U}(\theta, \varphi) = \text{CCX}[q_0, q_2, q_1] \text{CCU}_3[q_0, q_1, q_2](\vartheta = \theta, \lambda = -\varphi, \phi = \varphi) \text{CCX}[q_0, q_2, q_1], \quad (\text{A18})$$

where the first two qubits in the bracket are the controlled qubits and the last one is the target qubit. The CCX is the well-known Toffoli gate, and we just need to construct the CCU₃ gate. It turns out that the CCU₃ gate can be realized by the circuit shown in Fig. 6. Using these components, the quantum circuits for the chiral p -wave superconductors shown in Fig. 2(b) and (c) can be constructed. Using these components, the quantum circuit to measure each overlap for the chiral p -wave superconducting model requires ~ 60 CNOT gates on IBMQ machines.